CC10963 is being considered for publication in Physical Review C as a regular article.

High-spin structure of ^{96}Nb: A new level scheme and shell model insights
by J. Shi, Y. Zheng, C. B. Li, et al.

Dear NNDC data scientists,

his manuscript has been submitted to Physical Review C. We would appreciate your help with a data consistency check for this manuscript against the NNDC databases. – Thank you for offering this service!

For your information, the editorial process remains as follows:

- PRC is using its "referee" process to communicate with the NNDC.

- Please download the manuscript and submit the data report via

https://referees.aps.org/reviews/CC10963-16e7c4e-942931

- Please treat the manuscript with the same level of confidentiality that PRC expects referees to apply to such correspondence.

- Please return the data report with your findings via the referee server; please indicate that this is a data consistency check.

- If you wish to address any remarks solely to the editors, then please separate them clearly from the remarks that we can transmit to the authors.

- PRC will inform the authors about the outcome and send along your/the NNDC's findings (if any).

Please let us know if the data checking process will take more than about a week.

Thank you for your help.

Yours sincerely,

Christopher Wesselborg, Sc.D. (he/him/his)
Managing Editor
Physical Review C
Email: prc@aps.org

ADDITIONAL MATERIAL AVAILABLE (SEE FULL REFERRAL LETTER):

High-Spin Structure of ^{96}Nb: A New Level Scheme and Shell Model Insights

J. Shi (施婧),[1,2] Y. Zheng (郑云),[1,2,*] C. B. Li (李聪博),[1,2] T. X. Li (李天晓),[1] X. G. Wu (吴晓光),[1] R. Hong (洪锐),[1,3] S. X. Guan (关少雄),[1] H. Y. Wu (吴鸿毅),[2,4] M. Zheng (郑敏),[1] Z. H. Zhao (赵子豪),[1,5] Y. Q. Li (李韵秋),[1,2] Z. Y. He (贺子阳),[1] J. Z. Li (李金泽),[1] J. N. Zou (邹佳楠),[1] L. W. Yang (杨立旺),[1,6] Y. D. Fang (方永得),[7] J. H. Xu (徐君宏),[7] J. H. Li (黎健宏),[7] Z. H. Jia (贾子豪),[7] C. X. Jia (贾晨旭),[7] W. Q. Zhang (张文强),[7] J. L. Wang (汪金龙),[1] C. Y. Guo (郭成宇),[4] Z. X. Zhou (周振翔),[4] L. Ni (倪磊),[4] G. S. Li (李广顺),[7] B. Guo (郭冰),[1] S. Y. Wang (王守宇),[8,9] M. L. Liu (柳敏良),[7] C. Y. He (贺创业),[1] F. L. Liu (刘伏龙),[1] S. Wang (王硕),[8,9] D. P. Sun (孙大鹏),[8,9] and L. H. Zhu (竺礼华)[10]

[1]*Department of Nuclear Physics, China Institute of Atomic Energy, Beijing 102413, China*
[2]*Key Laboratory of Nuclear Data, China Institute of Atomic Energy, Beijing 102413, China*
[3]*Department of Science, Xihua University, Chengdu 610039, China*
[4]*School of Physics and State Key Laboratory of Nuclear Physics and Technology, Peking University, Beijing 100871, China*
[5]*Department of Physics, Jilin University, Changchun 130023, China*
[6]*School of Sciences Henan University of Technology, Zhengzhou 450001, China*
[7]*Institute of Modern Physics, Chinese Academy of Sciences, Lanzhou 730000, China*
[8]*School of Space Science and Physics, Institute of Space Sciences, Shandong University, Weihai 264209, China*
[9]*WeiHai Research Institute of Industrial Technology of Shandong University, Shandong University, Weihai 264209, China*
[10]*Physical and Nuclear Energy and Engineering, Beihang University, Beijing 100191,China*
(Dated: March 14, 2025)

High-spin states in ^{96}Nb have been investigated by using in-beam γ ray spectroscopy with the ^{82}Se(^{18}O,p3n)^{96}Nb reaction at beam energies of 82 and 88 MeV. Particle-γ-γ coincidence measurements employing CsI and HPGe arrays were utilized to enhance selectivity for Nb isotopic products. The decay sequences of previously known states have been extended to $I = (25^-)$ through the identification of fourteen new γ rays. The spin and parity of most γ rays in ^{96}Nb have been assigned for the first time using Angular Distribution of γ rays (ADO) and polarization analysis. The level structures in ^{96}Nb have been interpreted through shell model calculations employing the GWBXG and SNET interactions. The results indicate that the inclusion of proton core excitation relative to the Z=38 subshell closure is crucial for accurately describing the experimental high-spin states at $I \sim (18-25)\hbar$ with excitation energies above 6.2 MeV.

PACS numbers: 23.20.Lv, 25.70.Jj, 21.60.Cs, 27.60.+j

I. INTRODUCTION

Nuclei in the neutron-rich $A \approx 100$ region are generally challenging to be populated using fusion-evaporation reactions with stable beam-target combinations. Nuclear structure information for these nuclei is typically obtained through fusion-fission methods. However, this technique presents challenges in assigning spin and parity to excited states due to poor statistics and the lack of initial directional correlation information for the fission products. Therefore, it is proposed to utilize beam-target combinations with the highest neutron-to-proton ratios, such as ^{18}O+^{82}Se, and employ particle discrimination techniques to investigate reaction channels for specific neutron-rich isotopes near the stability line, aiming to explore their high-spin level structures.

Recent comprehensive studies by our collaborative research team have significantly advanced our understanding of the excited states of niobium isotopes, particularly in $^{90-94}$Nb [1–8], utilizing γ-ray spectroscopy and shell-model calculations. Our findings for ^{90}Nb [1, 8] demonstrate that both positive- and negative-parity states are accurately described by proton excitations within the fpg orbitals, combined with a single neutron hole in the $g_{9/2}$ orbital. The (16$^+$) state at 7035.8 keV is attributed to a neutron excitation across the $N = 50$ shell closure and a proton excitation in the $f_{5/2}$ orbital. For ^{91}Nb [2, 5], high-spin states arise from proton excitations spanning the $1p_{3/2}$, $1f_{5/2}$, and $1p_{1/2}$ orbitals to the $1g_{9/2}$ orbital, along with neutron excitations from the $1g_{9/2}$ orbital to the $1d_{5/2}$ or $1g_{7/2}$ orbitals, facilitated by the breaking of the $Z = 38$ and $N = 50$ core structures. In ^{92}Nb [3, 6], the high-spin states around $I \sim 18-20\hbar$ with excitation energies above 8.5 MeV can be fully described only when accounting for proton core excitation relative to the $Z = 38$ subshell closure and neutron particle-hole excitation for the $N = 50$ shell closure. In ^{93}Nb [4], low-lying states are predominantly driven by proton excitations across the $Z = 40$ subshell to the $1g_{9/2}$ orbital, while moderate-spin states involve neutron excitations across the $N = 56$ subshell. For high-spin states above 9.1 MeV, neutron excitation across the $N = 50$ shell closure becomes the dominant factor. In ^{94}Nb [7], the neutron $1h_{11/2}$ orbital play a significant role in understanding the structure. These studies offer deeper insights into the high-spin states of niobium isotopes, highlighting the importance of proton and neutron excitations across shell gaps and core excitations in determining their nuclear structure.

The odd-odd nucleus ^{96}Nb is located on the neutron-rich side of the stability line, specifically three neutrons away from the stable isotope ^{93}Nb. It is expected that an investigation into the high-spin states of ^{96}Nb will provide deeper and more valuable insights into the single-particle excitations of both

*Corresponding author. Email address: zhengyun@ciae.ac.cn

valence protons and neutrons, as well as the mechanism of core breaking.

The low-lying levels of ^{96}Nb have been previously investigated through (p, nγ) reactions [9, 10], yielding results for excitation energies up to 1.6 MeV. Higher excited states of this nucleus, with excitation energies reaching 2.96 MeV, were subsequently explored using one- and two-nucleon transfer reactions, including (t, α) [11], (^{3}He, t) [12, 13], (α, d) [14]. The high-spin structure of this nucleus was further examined through fusion-fission and multinucleon binary grazing reactions involving ^{24}Mg + ^{173}Yb [15], ^{23}Na + ^{176}Yb [15], ^{36}S + ^{176}Yb [16], ^{96}Zr + ^{124}Sn [16]. However, most excited states have not been assigned experimental spin and parity in the previous studies. Additionally, ambiguities regarding the placement of certain γ transitions persist in the level scheme [16].

This paper presents newly identified high-spin states in the ^{96}Nb nucleus. The spin and parity of all states have been determined and assigned based on directional correlation and polarization measurements. Additionally, the ^{96}Nb level scheme has been benchmarked against shell-model calculations using two effective interactions.

II. EXPERIMENTS

The experiment was performed at the HI-13 tandem accelerator in the China Institute of Atomic Energy (CIAE). Excited states of ^{96}Nb were populated via the heavy-ion fusion-evaporation reaction ^{82}Se(^{18}O, $p3n$)^{96}Nb at beam energies of 82 and 88 MeV. The target was a 0.85-mg/cm^2-thick isotopically enriched ^{82}Se metallic foil with a 4.45-mg/cm^2 Au backing to stop the recoiling nuclei. The γ rays emitted from the evaporation residues were detected using the Conjoint Gamma Array in China (CGAC), as shown in Fig. 1. The CGAC is composed of 12 Clover-type HPGe detectors and 28 n-type coaxial HPGe detectors, totaling 40 detectors, all equipped with BGO anti-Compton shielding. This array consists of 76 individual detection modules, each demonstrating an energy resolution between 2.0 keV and 2.8 keV at the 1332 keV. During the experiment, a total of twenty-nine Compton-suppressed HPGe detectors were arranged, with nine (five clover HPGe detectors) positioned at 90°, seven at 60°, eight at 120°, and six at 149°. The identification of in-beam γ transitions from charged particle channels has been to utilize coincidences between γ rays and light charged particles (p and α) to separate the transitions of interest from the much more intense background from xn channels. The evaporated charged particles were recorded using an approximately 4π charged particle detector array, which consists of 128 pieces of CsI crystals. The electronic signals generated from the interaction of γ rays and charged particles with the detectors were collected and processed with a general-purpose digital data acquisition system (GDDAQ), housed in two compact PCI/PXI crates and consisting of two 14-bit 250-MHz Pixie-16 modules and fourteen 14-bit 100-MHz Pixie-16 modules [17, 18].

All HPGe detectors were calibrated for energy and efficiency using the standard energy calibration γ-rays from the

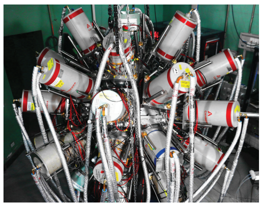

FIG. 1: Conjoint Gamma Array in China (CGAC).

decay of ^{60}Co, ^{133}Ba and ^{152}Eu radioactive sources. A total of 1.0×10^8 p-γ-γ coincidence data were accumulated in event-by-event mode. The recorded $\gamma - \gamma$ coincidence events were sorted into two-dimensional $E_\gamma - E_\gamma$ symmetric matrix, gated by the number of protons corresponding to Nb reaction channels, and then analyzed using the software package RADWARE [19].

To obtain information on the multipolarity of γ rays, two asymmetric matrices were constructed. The first axis (y axis) utilized the γ rays detected at all angles, while the second axis (x axis) included the γ rays detected at 149° and 90°, respectively. The angular distribution asymmetry (ADO) ratios, defined as $R_{\mathrm{ADO}}(\gamma) = I_\gamma(149^\circ)/I_\gamma(90^\circ)$, were derived from the γ ray coincidence intensities observed by the detectors at either 149° and 90°, utilizing gates set on the all-angles axis (y axis). For the present detector geometry, the typical R_{ADO} value for stretched quadrupole (or ΔI = 0 dipole) transitions was approximately ∼1.6, while for stretched pure dipole transitions, it was around 0.8.

In addition to ADO ratios, the unambiguous determination of multipolarities for γ transitions can be definitively derived from linear polarization measurements of observed γ-ray transitions. These measurements were conducted in coincidence using a clover detector, which served as a Compton polarimeter [20–22]. Data matrices were constructed with one axis denoting the energy recorded by all detectors, while the other axis corresponded to energy scattered either perpendicularly or parallel to the beam axis. The count of perpendicular $N_\perp$ and parallel $N_\parallel$ scatters for a specific γ-ray was ascertained by projecting the gated spectra. The asymmetry parameter (A_P) was subsequently calculated from these spectra applying the appropriate formula:

$$A_P = \frac{aN_\perp - N_\parallel}{aN_\perp + N_\parallel} \quad (1)$$

The value of a, representing the asymmetry of the clover array, was determined using data from the ^{133}Ba and ^{152}Eu radioactive sources.

The polarization (P) of γ radiation, the polarization sensitivity (Q), and the polarization asymmetry (A) are related through the equation ($P = \frac{A}{Q}$). The Q values for the array were adopted from Ref. [7]. A positive polarization asymmetry indicates an electric nature (stretched $E1$, $E2$) or non-stretched $M1$ transition, while a negative value characterizes a magnetic nature (stretched $M1$, $M2$) or non-stretched $E1$ transition. A value close to zero signifies the occurrence of a mixed transition. The current statistics for ^{96}Nb, which is derived from the weak p-reaction channel, allows for the determination of several linear polarization parameters for the strong transitions, as outlined in Table I. These findings offer crucial insights into parity changes and the electromagnetic nature of the linking transitions. Moreover, corroborating evidence from crossover or parallel transitions provides additional support for spin and multipolarity assignments.

III. THE LEVEL SCHEME

The level scheme of ^{96}Nb deduced in the present work is shown in Fig. 2. The placement of γ rays in the level scheme is based on the $\gamma-\gamma$ coincidence relations, γ-ray intensities, R_{ADO} values and polarization (P) measurements. The γ-ray intensities were determined from the total projection of the $p-\gamma-\gamma$ coincidence matrix. Spin and parity assignments are on the basis of $\gamma-\gamma$ directional correlations and deexcitation modes, or referenced from Ref [15, 16] for the ground and first excited states. Compared with the results reported in Refs [15, 16], the level scheme of ^{96}Nb was extended significantly in the present work. Fourteen new γ rays and eleven new states were identified and assigned in the present level scheme. The energies, relative intensities, polarization P and ADO ratios of γ rays as well as the spin and parity I^{π} assignments of levels are summarized in Table I. The typical coincidence γ ray spectra gated on the transitions of ^{96}Nb are shown in Figs. 3. Detailed experimental results are provided below.

Previous studies [9–16] have assigned spin-parities of 6^+ and (7^+) to the ground state and first excited state of ^{96}Nb, respectively. However, the spin and parity of the state above the (7^+) level at 222 keV were not determined in these works. The ADO and polarization analysis conducted in this study provides an opportunity to assign the spin and parity for high-spin states in ^{96}Nb. The R_{ADO} and P values for the 222-keV transition suggest a $M1+E2$ character. Consequently, the first excited state, depopulated by the 222-keV transition, has been confirmed to have a spin-parity of 7^+, thus supporting all prior tentative assignments. The experimentally measured R_{ADO} and polarization values for the 1164-keV transition are 0.54(8) and -0.10(22), respectively, indicative of a mixed multipolarity $M1+E2$ transition with a spin change of $\Delta I = 1$. The 1386-keV level has been conclusively assigned a spin-parity of $I^{\pi} = 8^+$. The observed R_{ADO} and polarization values of 0.91(36) and -0.22(64) for the 1656-keV transition support a mixed multipolarity $M1+E2$ transition. Consequently, the 1878-keV level, deexcitation via the 1656-keV transition, is determined to possess a spin-parities of $I^{\pi} = 8^+$. The 1527-keV transition has R_{ADO} and polarization values determined experimentally as 0.85(11) and 0.50(16) respectively, suggesting a pure $E1$ transition. This leads to the assignment of $I^{\pi} = 8^-$ for the 1749-keV level.

For the positive-parity part of the level scheme, most of the γ-rays reported in the previous studies [15, 16] were confirmed. As illustrated in Fig. 3 (a), nearly all transitions between these positive-parity states are observable. However, the 1343-keV transition identified by Brown *et al.* [16] in the positive sequence was not observed in the present study. Moreover, the 780- and 1480-keV transitions do not coincide with the 852-keV transition. Nevertheless, the 852-keV transition was observed in the γ-ray coincidence spectrum gated on the 918-keV and 745-keV transitions. The intensity of the 852-keV transition is stronger than that of the 918-keV transition. Consequently, the 852- and 918-keV transitions are positioned above the (10^+) state at 2131 keV, as shown in Fig. 2. Based on the experimentally measured R_{ADO} values of 1.50(30) and 0.88(27), the transitions at 852 keV and 918 keV are identified as $(E2)$ and $(M1+E2)$ multipolarity transitions, respectively. Consequently, the spin-parity assignments for the levels at 2983 keV and 3901 keV have been determined to be (12^+) and (13^+), respectively. While the polarization analysis for the 745-keV γ-ray was inconclusive, the significantly enhanced R_{ADO} parameter of 1.36(36) strongly supports an $E2$ multipolarity, indicating a spin change of $\Delta I = 2$. In parallel, the 825-keV transition shows R_{ADO} characteristics that are consistent with a stretched $\Delta I = 2$ transition. Furthermore, the newly observed 833-keV transition is illustrated in Fig. 3 (a). The latest R_{ADO} values and the established transition selection rules suggest that the spin and parity assignments for the 2964-, 2921-, 3051-, 3611-, and 4391-keV levels are likely (12^+), (11^+), (11^+), (12^+), and (14^+), respectively.

Regarding the negative-parity states, all the γ-rays below the 4545-keV level reported in previous studies [15, 16] have been verified, as shown in Fig. 3 (a)-(d). The analysis of the new R_{ADO} values and the corresponding transition selection rules points to the spin-parity assignments of (9^-), (10^-), (10^-), (11^-), (12^-) and (13^-) for the 1944-, 2377-, 2750-, 2954-, 3263-, and 3847-keV levels, respectively. With experimentally determined R_{ADO} and polarization values of 1.94(57) and 0.08(56) respectively, the 801-keV transition is consistent with an $E2$ multipolarity transition characterized by a spin change of $\Delta I = 2$. Therefore, it has been determined that the 4064-keV level possesses a spin-parity of $I^{\pi} = 14^-$. According to the newly obtained R_{ADO} value, the spin and parity of the 4545-keV level is likely (15^-).

The negative-parity states above the 4545-keV level have been newly identified. Thirteen new transitions, including six cascade $\Delta I = 2$ transitions, have been added, extending the excitation energy up to 10398 keV. The placement of these γ transitions was determined through analysis of individual γ-γ coincidence spectra and their respective intensities. Additional confirmation for the placement of these γ rays within the sequence was obtained by examining the energy sums. As demonstrated in Fig. 3 (a)-(d), all thirteen new transitions are visible in the gated spectrum. These new transitions primarily decay into the 15^- state via the 456-keV and 597-keV transitions. Experimental results indicate that the 1055-keV transi-

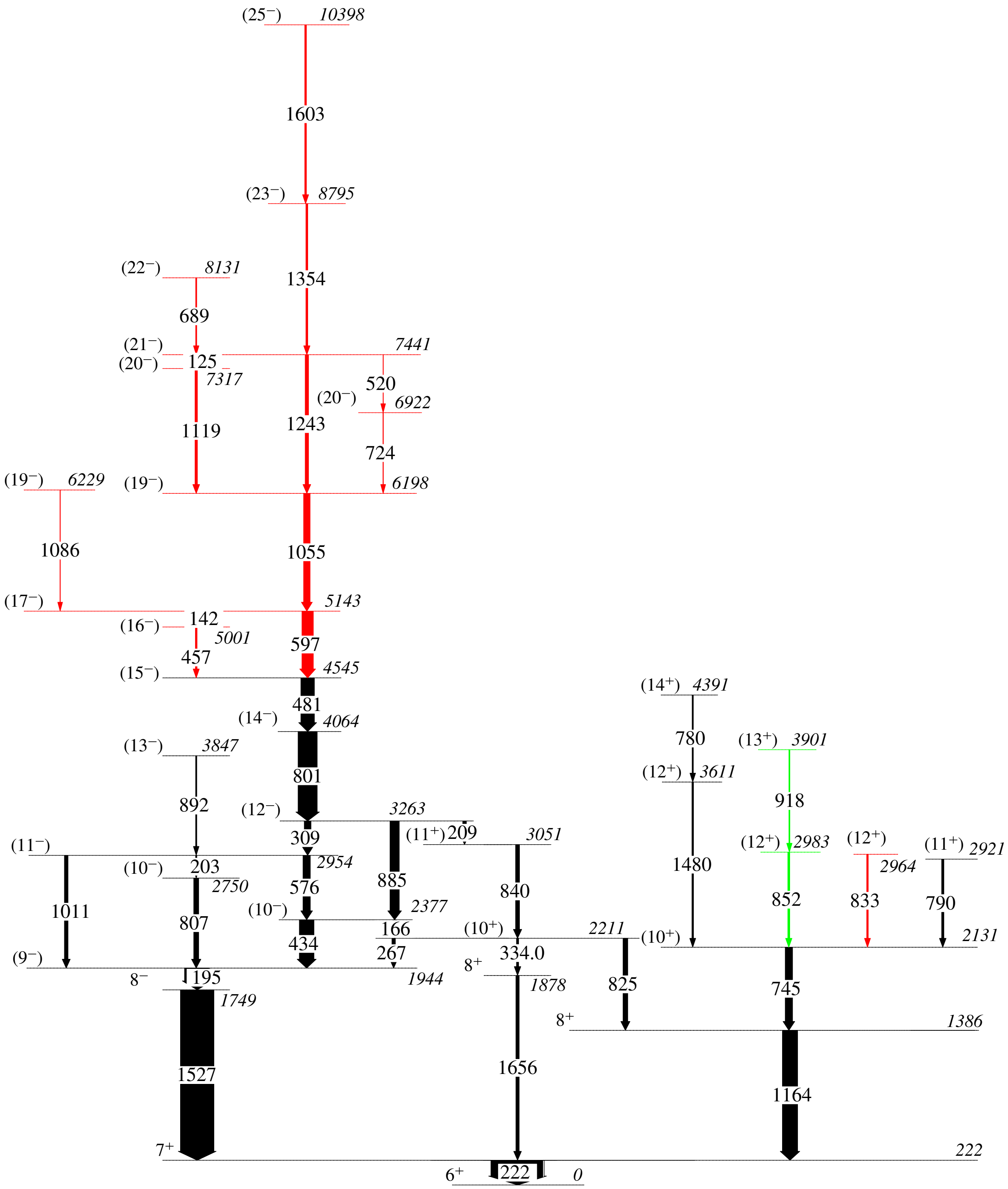

FIG. 2: The level scheme of ^{96}Nb established from the present work is shown. The energies of the observed excited states and γ-ray transitions are given in keV. The thicknesses of the arrows are roughly proportional to the γ-ray intensity listed in Table I. The new and rearranged γ rays are marked in red and green, respectively.

tion has an R_{ADO} value of 2.34(57), which is consistent with an $E2$ multipolarity transition. The observed R_{ADO} value of 1.72(54) for the 1243-keV transition support an $E2$ multipolarity transition with a spin change of $\Delta I = 2$. Furthermore, considering the dipole nature of the 457-, 142-, 724-, 520-, 1119-, 125-, and 689-keV transitions and the quadrupole nature of the 597-, 1055-, 1086-, 1243-, 1354-, and 1603-keV transitions, the assignments of $I^\pi = (16^-), (17^-), (19^-), (19^-), (20^-), (20^-), (21^-), (22^-), (23^-)$, and (25^-) for the 5001-, 5143-, 6198-,6229-, 6922-, 7317-, 7441-, 8131-, 8795-, and 10398-keV levels, respectively, were suggested for the negative-parity sequence.

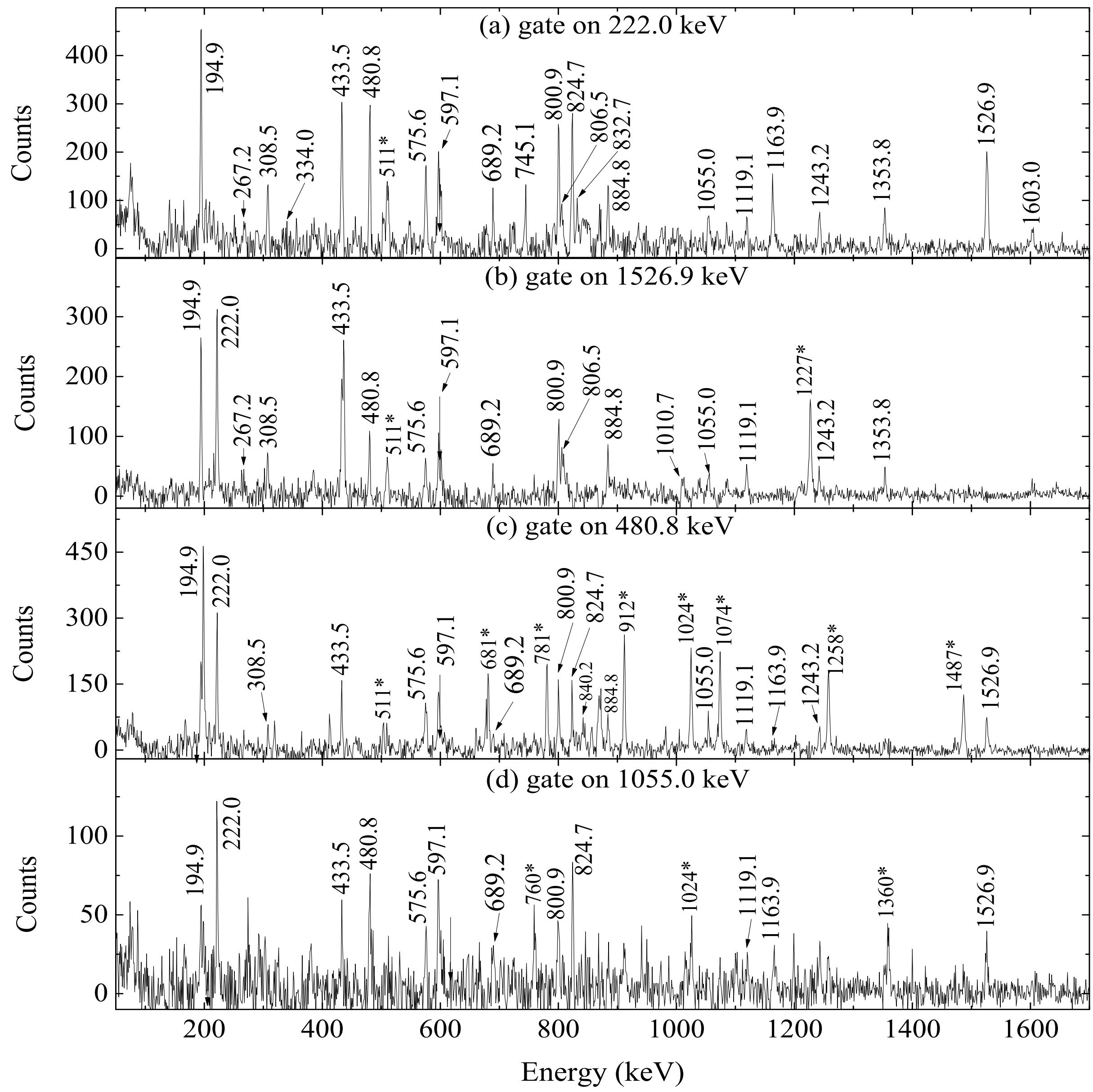

FIG. 3: Representative spectrums obtained by gating on (a) 222.0 keV, (b) 1526.9 keV, (c) 480.8 keV, and (d) 1055.0 keV transitions in the symmetric γ-γ coincidence matrix, in coincidence with the protons detected in the CsI ball. The main coincidence γ rays are labeled with its energies in keV. Transitions marked with asterisks, as well as those not labeled by energy, are attributed to contaminant lines close to the gating energies.

IV. DISCUSSION

The level scheme depicted in Fig. 2 reveals several high-energy γ transitions around 1.5 MeV, indicating nucleon excitation across a significant energy (shell) gap. For instance, the high-energy γ transitions, such as (19^-) (6198 keV) $\rightarrow$ (17^-) (5143 keV), (21^-) (7441 keV) $\rightarrow$ (19^-) (6198 keV), (23^-) (8795 keV) $\rightarrow$ (21^-) (7441 keV), and (25^-) (10398 keV) $\rightarrow$ 23^- (8795 keV), could be attributed to proton excitation across the $Z = 38$ gap. These transitions suggest changes in intrinsic structure due to such excitations. To verify this hypothesis, calculations were performed incorporating the proton excitations across the Z=38 subshell gap. The isotones ^{93}Sr [24] and ^{97}Mo [25], along with the isotopes $^{90-97,99}$Nb [1–8, 16, 24, 26], were systematically investigated using the shell model. These studies demonstrate that promoting protons from the *pf* orbits into the *g* orbit is sufficient to describe the low-spin states. For high-spin states, it is proposed to consider proton or neutron core excitation through the Z=38 or N=50 subshell or shell closure.

To elucidate the decay sequences observed in ^{96}Nb, we conducted shell-model calculations using the nushellx computational framework [27], employing two different interactions. Specifically, the theoretical approach utilizes the GWB model

TABLE I: Level excitation energy E_x, energies E_γ, relative intensities, R_{ADO} ratios, polarization P, initial- and final-state spin-parities, and multipolarities of γ-ray transitions assigned to ^{96}Nb in the present work.

E_x (keV)	E_γ (keV)	$I_\gamma{}^a$	R_{ADO}	Polarization(P)	$I_i^\pi \to I_f^{\pi b}$	Mult.
222.0	222.0(2)	155	0.67(11)	-0.51(22)	$7^+ \to 6^+$	$M1+E2$
1385.9	1163.9(3)	45.3(61)	0.54(8)	-0.10(22)	$8^+ \to 7^+$	$M1+E2$
1748.9	1526.9(2)	100.0(44)	0.85(11)	0.50(16)	$8^- \to 7^+$	$E1$
1877.5	1655.5(7)	9.7(40)	0.91(36)	-0.22(64)	$8^+ \to 7^+$	$M1+E2$
1943.8	194.9(2)	72.5	0.53(8)		$9^{(-)} \to (8^-)$	$(M1+E2)$
2131.0	745.1(2)	21.8(24)	1.36(36)		$10^{(+)} \to (8^+)$	$E2$
2211.0	267.2(2)	9.6(42)			$(10^+) \to 9^{(-)}$	$(E1)$
	334.0(4)	6.2(9)			$(10^+) \to (8^+)$	$(E2)$
	824.7(4)	14.0(55)	1.78(43)		$(10^+) \to (8^+)$	$(E2)$
2377.3	165.5(4)	7.8(16)			$(10^-) \to (10^+)$	$(E1)$
	433.5(2)	43.4(35)	0.83(15)		$(10^-) \to 9^{(-)}$	$(M1+E2)$
2750.3	806.5(4)	14.6(36)	0.83(16)		$(10^-) \to 9^{(-)}$	$(M1+E2)$
2920.8	789.8(7)	6.6(17)	1.09(53)		$(11^+) \to 10^{(+)}$	$(M1+E2)$
2954.5	202.7(5)	3.6(6)	0.58(8)		$(11^-) \to (10^-)$	$(M1+E2)$
	575.6(2)	21.7(79)	1.17(27)		$(11^-) \to (10^-)$	$(M1+E2)$
	1010.7(5)	4.8(18)	1.54(45)		$(11^-) \to 9^{(-)}$	$(E2)$
2963.7	832.7(3)	4.6(29)	1.72(64)		$(12^+) \to 10^{(+)}$	$(E2)$
2982.8	851.8(5)	5.8(20)	1.50(30)			$(E2)$
3051.2	840.2(7)	11.6(28)	1.09(37)		$(11^+) \to (10^+)$	$(M1+E2)$
3263.0	208.6(3)	10.8(18)	0.59(35)		$(12^-) \to (11^+)$	$(E1)$
	308.5(2)	19.8(33)	0.82(48)		$(12^-) \to (11^-)$	$(M1+E2)$
	884.8(2)	27.6(32)	1.62(34)		$(12^-) \to (10^-)$	$(E2)$
3611.2	1480.2(2)	4.8(14)	1.54(20)		$(12^+) \to 10^{(+)}$	$(E2)$
3846.9	892.4(7)	3.4(7)	1.38(38)		$(13^-) \to (11^-)$	$(E2)$
3900.9	918.1(5)	2.9(19)	0.88(27)			$(M1+E2)$
4063.9	800.9(2)	57.0(54)	1.94(57)	0.08(56)	$(14^-) \to (12^-)$	$E2$
4391.4	780.2(2)	3.5(7)	1.86(82)		$(14^+) \to (12^+)$	$(E2)$
4544.7	480.8(2)	40.1(36)	1.14(17)		$(15^-) \to (14^-)$	$(M1+E2)$
5001.4	456.7(4)	5.1(4)	0.38(21)		$(16^-) \to (15^-)$	$(M1+E2)$
5143.1	141.7(4)	3.5(15)	0.56(28)		$(17^-) \to (16^-)$	$(M1+E2)$
	597.1(3)	34.0(62)			$(17^-) \to (15^-)$	$(E2)$
6198.1	1055.0(4)	19.4(42)	2.34(57)		$(19^-) \to (17^-)$	$(E2)$
6229.0	1085.9(2)	1.0(1)	0.79(32)		$(18^-) \to (17^-)$	$(M1+E2)$
6922.0	723.9(4)	1.3(1)	1.19(35)		$(20^-) \to (19^-)$	$(M1+E2)$
7317.2	1119.1(2)	7.1(19)	1.06(46)		$(20^-) \to (19^-)$	$(M1+E2)$
7441.3	124.9(6)	1.8(2)			$(21^-) \to (20^-)$	$(M1+E2)$
	519.8(2)	<1			$(21^-) \to (20^-)$	$(M1+E2)$
	1243.2(7)	10.0(13)	1.72(54)		$(21^-) \to (19^-)$	$(E2)$
8130.5	689.2(4)	3.1(6)	1.00(18)		$(22^-) \to (21^-)$	$(M1+E2)$
8795.1	1353.8(4)	5.5(18)	1.51(49)		$(23^-) \to (21^-)$	$(M1+E2)$
10398.1	1603.0(4)	4.9(19)	1.61(57)		$(25^-) \to (23^-)$	$(E2)$

[a] Intensities are normalized to the 1526.9-keV transition with I_γ=100.

[b] Excitation energies of initial E_i and final E_f states.

space in conjunction with the GWBXG effective interaction, comprising four proton orbitals ($1f_{5/2}$, $2p_{3/2}$, $2p_{1/2}$, $1g_{9/2}$) and six neutron orbits ($2p_{1/2}$, $1g_{9/2}$, $1g_{7/2}$, $2d_{5/2}$, $2d_{3/2}$, $3s_{1/2}$) relative to the doubly magic ^{66}Ni core. As established in prior studies [28–32], the single-particle energies (SPEs) relative to the ^{66}Ni core were parametrized as follows: $\varepsilon^{\pi}_{1f_{5/2}}$=-5.322 MeV, $\varepsilon^{\pi}_{2p_{3/2}}$=-6.144 MeV, $\varepsilon^{\pi}_{2p_{1/2}}$=-3.941 MeV, $\varepsilon^{\pi}_{1g_{9/2}}$=-1.250 MeV, $\varepsilon^{\nu}_{2p_{1/2}}$=-0.696 MeV, $\varepsilon^{\nu}_{1g_{9/2}}$=-2.597 MeV, $\varepsilon^{\nu}_{1g_{7/2}}$=5.159 MeV, $\varepsilon^{\nu}_{2d_{5/2}}$=1.830 MeV, $\varepsilon^{\nu}_{2d_{3/2}}$=4.261 MeV, and $\varepsilon^{\nu}_{3s_{1/2}}$=1.741 MeV. These SPE parameters, combined with optimized residual interaction strengths derived from systematic fitting procedures, were subsequently used in the configuration-interaction calculations to determine nuclear level energies.

The nucleus ^{96}Nb contains 13 valence protons and 17 valence neutrons within the considered configuration space. Due to the extensive dimensions of the valence space, truncations were implemented in our calculations, as referenced in Refs. [7, 33]. Four protons were allowed to be excited from the lower-energy $1f_{5/2}$ and $2p_{3/2}$ orbitals to the higher-energy $2p_{1/2}$ and $1g_{9/2}$ orbitals, crossing the Z = 38 subshell gap. In contrast, neutron excitations from lower-energy orbitals to

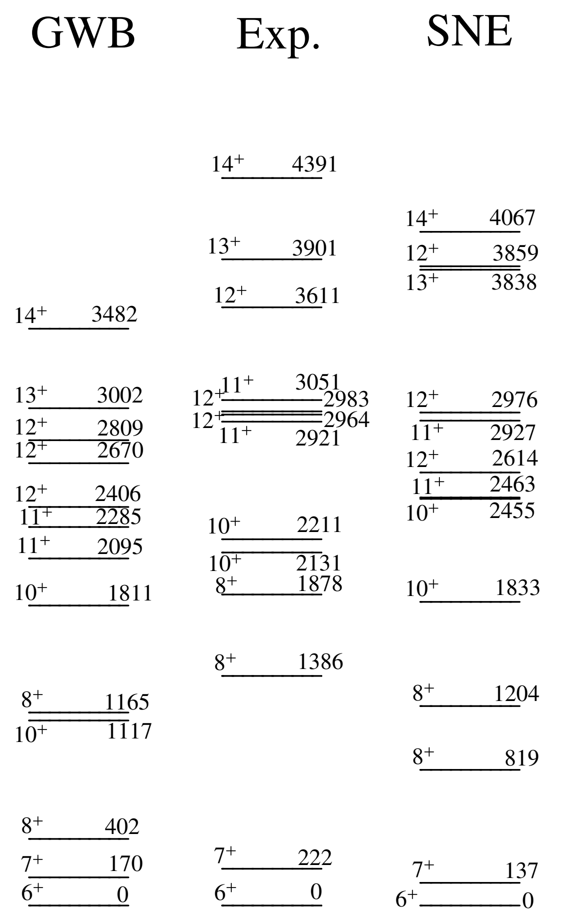

FIG. 4: Comparison of experimental excitation energies in ^{96}Nb (π=+) with shell-model predictions with the model spaces GWB and SNE.

higher-energy orbitals across the $N = 50$ shell gap were not permitted.

Based on shell-model calculations using the GWBXG interaction, the high-spin states in ^{96}Nb identified in this study can primarily be attributed to four distinct mechanisms: (a) excitation of either one proton or a proton pair from the fully occupied $2p_{1/2}$ orbit to the $1g_{9/2}$ orbit; (b) excitation of protons from the fully filled $1f_{5/2}$, $2p_{3/2}$ subshells to the $1g_{9/2}$ orbit; (c) valence neutron excitation from the $2d_{5/2}$ orbit to the $1g_{7/2}$ orbit; and (d) neutron excitation from the $2d_{5/2}$ orbit to the $3s_{1/2}$ orbit. These excitation mechanisms have been used to elucidate the observed states of ^{96}Nb.

The calculated energy levels of ^{96}Nb are compared with the experimental data in Figs. 4 and 5. To investigate the structural properties of the positive- and negative-parity sequences, the primary components of the wave functions for each state are detailed in Tables II and III. These components are characterized by one to three dominant configurations that significantly contribute to the overall wave function.

The $I^{\pi} = 6^{+}$ ground state is predominantly generated by the coupling of one $1g_{9/2}$ proton with an unpaired neutron in the $2d_{5/2}$ orbital. The configuration dominated by a single

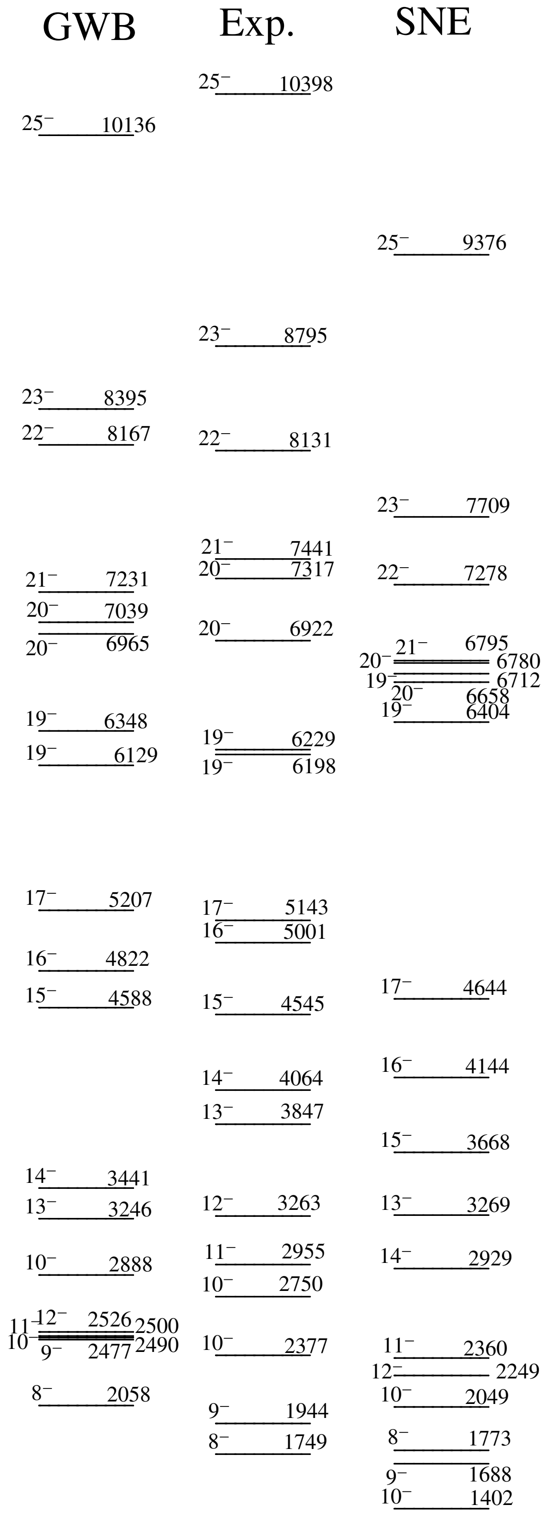

FIG. 5: Comparison of experimental excitation energies in ^{96}Nb (π=-) with shell-model predictions with the model spaces GWB and SNE.

$1g_{9/2}$ proton coupled to a valence neutron in the $1g_{7/2}$ orbital predominantly results in the first excited state with $I^{\pi}=7^{+}$. The calculated excitation energies for the positive parity states with spins $I^{\pi}=6^{+}$ and $I^{\pi}=7^{+}$ are in reasonable agreement with experimental results. For the $I^{\pi}=8^{+}_{1}$ to $I^{\pi}=14^{+}_{1}$ states, the calculated energies are 400 to 1014 keV lower than the experimental values. However, the differences between the calculated energy gaps and observed γ transitions range from 30 to 584 keV. Specifically, the differences for the transitions $10^{+}_{1}\rightarrow 8^{+}_{1}$ and $14^{+}_{1}\rightarrow 12^{+}_{3}$ are just 30 and 107 keV, respectively. The configurations $\pi(1g_{9/2})\otimes\nu(1g_{7/2}/2d_{5/2})^{5}$ and $\pi(1g_{9/2})^{3}\otimes\nu(1g_{7/2}/2d_{5/2})^{5}$ play a dominant role in the formation of the $I^{\pi}=8^{+}_{1}$ to $I^{\pi}=14^{+}$ excited state.

The calculated lowest-lying 8^{-}_{1}, 9^{-}_{1}, 10^{-}_{1}, and 10^{-}_{2} states are 100-500 keV higher than the experimental ones. In contrast, all other negative parity states are predicted to be at the same or lower energies. The calculations predict that the yrast 8^{-}_{1} to 16^{-}_{1} states share the configuration $\pi[(2p_{1/2})^{1}(1g_{9/2})^{2}]\otimes\nu(1g_{7/2}/2d_{5/2})^{5}$. However, the 10^{-}_{2} state involves the excitation of two protons from the $1f_{5/2}$ and $2p_{1/2}$ into $1g_{9/2}$ orbital. Additionally, a pair of neutrons is removed from the $2d_{5/2}$ orbital and transferred to the $3s_{1/2}$ orbital.

The 19^{-}_{1} to 23^{-}_{1} states, except for 19^{-}_{2}, involve the excitation of one proton across the shell gap at Z=38 into the $1g_{9/2}$ orbital. Consequently, a gap of approximately 1-1.5 MeV is predicted for the transition $19^{-}_{1}\rightarrow 17^{-}_{1}$, $19^{-}_{2}\rightarrow 17^{-}_{1}$, $20^{-}_{2}\rightarrow 19^{-}_{1}$, $21^{-}_{1}\rightarrow 19^{-}_{1}$, and $23^{-}_{1}\rightarrow 21^{-}_{1}$. Notably, 20^{-}_{1} and 22^{-}_{1} states involve one neutron excited from the $2d_{5/2}$ or $1g_{7/2}$ orbital to the $3s_{1/2}$ orbital. The primary configuration of the states from 19^{-}_{1} to 23^{-}_{1} is $\pi[(1f_{5/2})^{-1}(1g_{9/2})^{4}]\otimes\nu(1g_{7/2}/2d_{5/2})^{5}$ or $\pi[(1f_{5/2})^{-1}(1g_{9/2})^{4}]\otimes\nu[(1g_{7/2}/2d_{5/2})^{4}(3s_{1/2})^{1}]$, as shown in Table II. The larger gap spacing (1603 keV) between the 25^{-}_{1} and 23^{-}_{1} states is likely due to the excitation of a pair of $1f_{5/2}$ protons into the $1g_{9/2}$ orbital, crossing the $Z=38$ subshell closure.

The structure of the ^{96}Nb nucleus is expected to be influenced by variations in neutron number, particularly as the high-j $1h_{11/2}$ orbital begin to fill in Nb isotopes with increasing neutron number. Previous studies have indicated the impact of the $1h_{11/2}$ neutron orbital on the level structure of isotopes in this mass region, including Rb [34], Sr [35–39], Y [40], Zr [41–43], and Nb [7]. Consequently, shell model calculations for ^{96}Nb were performed utilizing the SNET interaction and an expanded SNE configuration model space, which encompasses eight proton orbits ($1f_{5/2}$, $2p_{3/2}$, $2p_{1/2}$, $1g_{9/2}$, $1g_{7/2}$, $2d_{5/2}$, $2d_{3/2}$, $3s_{1/2}$) and nine neutron orbits ($1f_{5/2}$, $2p_{3/2}$, $2p_{1/2}$, $1g_{9/2}$, $1g_{7/2}$, $2d_{5/2}$, $2d_{3/2}$, $3s_{1/2}$, $1h_{11/2}$) above an inert ^{56}Ni core. The single-particle energies utilized in this interaction were established as follows: $\varepsilon^{\pi}_{1f_{5/2}}$=0.525 MeV, $\varepsilon^{\pi}_{2p_{3/2}}$=1.228 MeV, $\varepsilon^{\pi}_{2p_{1/2}}$=5.106 MeV, $\varepsilon^{\pi}_{1g_{9/2}}$=5.518 MeV, $\varepsilon^{\pi}_{1g_{7/2}}$=20.656 MeV, $\varepsilon^{\pi}_{2d_{3/2}}$=20.016 MeV, $\varepsilon^{\pi}_{3s_{1/2}}$=6.895 MeV, $\varepsilon^{\nu}_{1f_{5/2}}$=0 MeV, $\varepsilon^{\nu}_{2p_{3/2}}$=0 MeV, $\varepsilon^{\nu}_{2p_{1/2}}$=0 MeV, $\varepsilon^{\nu}_{1g_{9/2}}$=0 MeV, $\varepsilon^{\nu}_{1g_{7/2}}$=4.352 MeV, $\varepsilon^{\nu}_{2d_{5/2}}$=2.313 MeV, $\varepsilon^{\nu}_{2d_{3/2}}$=3.440 MeV, $\varepsilon^{\nu}_{3s_{1/2}}$=1.532 MeV, and $\varepsilon^{\nu}_{1h_{11/2}}$=-0.589 MeV [44]. To en-

TABLE II: Main partitions of the wave functions for ^{96}Nb within the GWB model space. $\pi\otimes\nu$ represents $\pi(1f_{5/2}, 2p_{3/2}, 2p_{1/2}, 1g_{9/2})\otimes\nu(1g_{7/2}, 2d_{5/2}, 2d_{3/2}, 3s_{1/2})$

E_{calc} (keV)	J^{π}_{i}	Configurations ($\pi\otimes\nu$)	
		%	Leading config.
0	6^{+}_{1}	66.3	$(6,4,2,1)\otimes(0,5,0,0)$
170	7^{+}_{1}	11.9	$(6,4,0,3)\otimes(1,4,0,0)$
		10.1	$(6,4,0,3)\otimes(1,2,0,2)$
		7.8	$(4,4,2,3)\otimes(1,4,0,0)$
402	8^{+}_{1}	25.1	$(6,4,2,1)\otimes(1,4,0,0)$
		10.7	$(6,4,0,3)\otimes(1,4,0,0)$
1165	8^{+}_{2}	35.2	$(6,4,2,1)\otimes(1,4,0,0)$
1117	10^{+}_{1}	36.3	$(6,4,2,1)\otimes(1,4,0,0)$
		7.5	$(6,4,0,3)\otimes(1,4,0,0)$
		6.7	$(6,4,2,1)\otimes(1,3,0,1)$
1811	10^{+}_{2}	28.9	$(6,4,2,1)\otimes(1,4,0,0)$
2095	11^{+}_{1}	12.1	$(6,4,2,1)\otimes(1,4,0,0)$
		8.0	$(6,4,0,3)\otimes(1,3,0,1)$
		6.5	$(6,4,0,3)\otimes(1,4,0,0)$
2285	11^{+}_{2}	20.9	$(6,4,2,1)\otimes(1,4,0,0)$
2406	12^{+}_{1}	47.1	$(6,4,2,1)\otimes(1,4,0,0)$
		7.8	$(6,4,0,3)\otimes(1,4,0,0)$
		5.7	$(6,2,2,3)\otimes(1,4,0,0)$
2670	12^{+}_{2}	9.3	$(6,4,2,1)\otimes(1,4,0,0)$
		4.8	$(6,4,0,3)\otimes(1,4,0,0)$
2809	12^{+}_{3}	16.8	$(6,4,0,3)\otimes(2,3,0,0)$
		9.6	$(4,4,2,3)\otimes(2,3,0,0)$
3002	13^{+}_{1}	17.8	$(6,4,0,3)\otimes(2,3,0,0)$
		9.4	$(4,4,2,3)\otimes(2,3,0,0)$
3482	14^{+}_{1}	19.5	$(6,4,0,3)\otimes(1,4,0,0)$
		8.0	$(4,4,2,3)\otimes(1,4,0,0)$
2058	8^{-}_{1}	25.9	$(6,4,1,2)\otimes(1,4,0,0)$
		7.9	$(5,4,2,2)\otimes(1,4,0,0)$
2477	9^{-}_{1}	19.9	$(6,4,1,2)\otimes(1,4,0,0)$
		6.5	$(6,4,1,2)\otimes(1,3,0,1)$
2490	10^{-}_{1}	37.0	$(6,4,1,2)\otimes(1,4,0,0)$
		8.1	$(6,4,1,2)\otimes(0,4,1,0)$
2888	10^{-}_{2}	9.6	$(5,4,0,4)\otimes(1,2,0,2)$
		7.4	$(5,4,0,4)\otimes(1,4,0,0)$
2500	11^{-}_{1}	37.2	$(6,4,1,2)\otimes(1,4,0,0)$
		17.9	$(6,3,2,2)\otimes(1,4,0,0)$
2526	12^{-}_{1}	52.5	$(6,4,1,2)\otimes(1,4,0,0)$
		10.1	$(6,4,1,2)\otimes(1,2,0,2)$
3246	13^{-}_{1}	36.5	$(6,4,1,2)\otimes(1,4,0,0)$
		17.9	$(6,4,1,2)\otimes(1,3,0,1)$
		12.1	$(6,3,2,2)\otimes(1,4,0,0)$
3441	14^{-}_{1}	48.6	$(6,4,1,2)\otimes(1,4,0,0)$
		18.4	$(6,4,1,2)\otimes(1,3,0,1)$
4588	15^{-}_{1}	36.7	$(6,4,1,2)\otimes(1,4,0,0)$
		11.8	$(5,4,2,2)\otimes(1,4,0,0)$
		9.3	$(6,4,1,2)\otimes(1,3,0,1)$
4822	16^{-}_{1}	49.0	$(6,4,1,2)\otimes(1,4,0,0)$
		11.7	$(6,4,1,2)\otimes(1,2,0,2)$
5207	17^{-}_{1}	63.4	$(6,4,1,2)\otimes(2,3,0,0)$
6129	19^{-}_{1}	21.1	$(5,4,0,4)\otimes(2,3,0,0)$
		15.5	$(4,4,1,4)\otimes(2,3,0,0)$
6348	19^{-}_{2}	58.1	$(6,4,1,2)\otimes(2,3,0,0)$
		14.9	$(6,4,1,2)\otimes(2,2,0,1)$
6965	20^{-}_{1}	12.5	$(5,4,0,4)\otimes(2,2,0,1)$
		8.1	$(4,4,1,4)\otimes(2,2,0,1)$

Table II. (*Continued*)

E_{calc} (keV)	J_i^{π}	Configurations ($\pi \otimes \nu$)	
		%	Leading config.
7039	20_2^-	16.8	$(5,4,0,4)\otimes(2,3,0,0)$
		9.4	$(5,4,0,4)\otimes(2,2,0,1)$
		8.7	$(4,4,1,4)\otimes(2,3,0,0)$
7231	21_1^-	21.6	$(4,4,1,4)\otimes(2,3,0,0)$
		19.7	$(5,4,0,4)\otimes(2,3,0,0)$
8167	22_1^-	14.1	$(5,4,0,4)\otimes(2,2,0,1)$
		10.4	$(5,4,0,4)\otimes(2,3,0,0)$
8395	23_1^-	22.9	$(5,4,0,4)\otimes(2,3,0,0)$
		17.6	$(5,4,0,4)\otimes(2,1,0,2)$
		15.9	$(4,4,1,4)\otimes(2,3,0,0)$
10136	25_1^-	54.1	$(4,4,1,4)\otimes(2,3,0,0)$
		10.2	$(4,3,2,4)\otimes(2,3,0,0)$

sure computational tractability, consistent truncation schemes were systematically implemented across the model space. Specifically, proton excitations were limited to a maximum of four particles crossing the Z=38 subshell closure, while neutron excitations across the N=50 major shell gap were strictly prohibited in low-energy orbitals. Five neutrons are allowed to be excited from the $2d_{5/2}$ orbital to the $1g_{7/2}$, $2d_{3/2}$ and $3s_{1/2}$ orbitals. Furthermore, the configuration space allowed one neutron to occupy the high-spin $1h_{11/2}$ orbital.

Similarly, based on shell-model calculations using the SNET interaction, the high-spin states in ^{96}Nb identified in this study can primarily be attributed to three distinct mechanisms: (a) the excitation of a proton pair from the fully occupied $2p_{1/2}$ orbital to the $1g_{9/2}$ orbital; (b) the excitation of valence neutrons from the $2d_{5/2}$ orbital to the $1g_{7/2}$ orbital; and (c) the excitation of neutrons from the $2d_{5/2}$ orbital to the $2d_{3/2}$, $3s_{1/2}$, and $1h_{11/2}$ orbits.

As shown in Fig. 4, the calculated excitation energies for the positive parity states are in reasonable agreement with the experimental results. The first discrepancy is that the energy gap between the 10_2^+ and 11_1^+ is not observed in the calculation results, with the difference being just 8 keV. Additionally, the difference between the 12_1^+ and 12_2^+ states is much larger than the experimental ones. The primary contributions to the 6_1^+ to 13_1^+ states obtained in the shell model arise from one proton in the $1g_{9/2}$ orbital coupled with five neutrons in the $2d_{5/2}$, $1g_{7/2}$, $2d_{3/2}$, and $3s_{1/2}$ orbitals. The calculations predict that the 14_1^+ state includes excitation of one proton from the $2p_{1/2}$ orbital into the $1g_{9/2}$ orbital, as well as the excitation of one neutron from the $1g_{7/2}$ or $2d_{5/2}$ orbital to the $1h_{11/2}$ orbital.

The calculated energy gaps between the negative states largely reproduce the energies of the observed γ-rays, with differences ranging from approximately 64 to 719 keV. It should be noted that the sequences of calculated 19_2^- and 20_1^-, 13_1^- and 14_1^-, 11_1^- and 12_1^-, 9_1^- and 10_1^-, as well as 8_1^- and 9_1^- are reversed compared to the experimental results. The calculated 8_1^- to 14_1^- states predominantly involve $\pi(1g_{9/2})^1 \otimes \nu[(2d_{5/2})^{-1}(1h_{11/2})^1]$ configurations. The 15_1^- and 16_1^- states share the same proton configuration as the

TABLE III: Main partitions of the wave functions for ^{96}Nb within the SNE model space. $\pi\otimes\nu$ represents $\pi(1f_{5/2}, 2p_{3/2}, 2p_{1/2}, 1g_{9/2})\otimes\nu(1g_{7/2}, 2d_{5/2}, 2d_{3/2}, 3s_{1/2}, 1h_{11/2})$

E_{calc} (keV)	J_i^{π}	Configurations ($\pi \otimes \nu$)	
		%	Leading config.
0	6_1^+	53.9	$(6,4,2,1)\otimes(0,5,0,0,0)$
137	7_1^+	53.3	$(6,4,2,1)\otimes(0,5,0,0,0)$
819	8_1^+	65.6	$(6,4,2,1)\otimes(0,4,0,1,0)$
1204	8_2^+	39.2	$(6,4,2,1)\otimes(1,4,0,0,0)$
		9.7	$(6,4,0,3)\otimes(1,4,0,0,0)$
1833	10_1^+	38.9	$(6,4,2,1)\otimes(1,4,0,0,0)$
		16.5	$(6,4,2,1)\otimes(1,3,0,1,0)$
2455	10_2^+	26.1	$(6,4,2,1)\otimes(0,4,1,0,0)$
		22.1	$(6,4,2,1)\otimes(1,3,0,1,0)$
2463	11_1^+	53.2	$(6,4,2,1)\otimes(1,4,0,0,0)$
		10.5	$(6,4,0,3)\otimes(1,4,0,0,0)$
2927	11_2^+	43.6	$(6,4,2,1)\otimes(1,3,0,1,0)$
		10.5	$(6,4,0,3)\otimes(1,3,0,1,0)$
2614	12_1^+	58.1	$(6,4,2,1)\otimes(1,4,0,0,0)$
		10.7	$(6,4,0,3)\otimes(1,4,0,0,0)$
2976	12_2^+	58.5	$(6,4,2,1)\otimes(1,3,0,1,0)$
		12.0	$(6,4,0,3)\otimes(1,3,0,1,0)$
3859	12_3^+	15.1	$(6,4,2,1)\otimes(1,3,0,1,0)$
		14.2	$(6,4,2,1)\otimes(2,3,0,0,0)$
		12.7	$(6,4,0,3)\otimes(2,3,0,0,0)$
3838	13_1^+	25.2	$(6,4,2,1)\otimes(1,3,0,1,0)$
		12.5	$(6,4,2,1)\otimes(2,3,0,0,0)$
4067	14_1^+	34.1	$(6,4,1,2)\otimes(0,4,0,0,1)$
		8.1	$(6,4,1,2)\otimes(0,2,0,2,1)$
		7.4	$(6,4,1,2)\otimes(2,2,0,0,1)$
1773	8_1^-	43.3	$(6,4,2,1)\otimes(0,4,0,0,1)$
		6.1	$(6,4,0,3)\otimes(0,4,0,0,1)$
1688	9_1^-	44.7	$(6,4,2,1)\otimes(0,4,0,0,1)$
		11.3	$(6,4,2,1)\otimes(0,3,0,1,1)$
1402	10_1^-	39.1	$(6,4,2,1)\otimes(0,4,0,0,1)$
		7.5	$(6,4,2,1)\otimes(0,2,0,2,1)$
		6.3	$(6,4,0,3)\otimes(0,4,0,0,1)$
2049	10_2^-	43.0	$(6,4,2,1)\otimes(0,4,0,0,1)$
		15.3	$(6,4,2,1)\otimes(0,3,0,1,1)$
2360	11_1^-	37.5	$(6,4,2,1)\otimes(0,4,0,0,1)$
		21.3	$(6,4,2,1)\otimes(0,3,0,1,1)$
2249	12_1^-	32.4	$(6,4,2,1)\otimes(0,4,0,0,1)$
		19.4	$(6,4,2,1)\otimes(0,3,0,1,1)$
3269	13_1^-	32.2	$(6,4,2,1)\otimes(0,4,0,0,1)$
2929	14_1^-	30.8	$(6,4,2,1)\otimes(0,4,0,0,1)$
		24.5	$(6,4,2,1)\otimes(0,3,0,1,1)$
3668	15_1^-	32.2	$(6,4,2,1)\otimes(1,3,0,0,1)$
		12.0	$(6,4,0,3)\otimes(1,3,0,0,1)$
		7.5	$(6,4,2,1)\otimes(1,2,0,1,1)$
4144	16_1^-	34.3	$(6,4,2,1)\otimes(1,3,0,0,1)$
		13.3	$(6,4,0,3)\otimes(1,3,0,0,1)$
4644	17_1^-	25.3	$(6,4,2,1)\otimes(1,2,0,1,1)$
		22.8	$(6,4,2,1)\otimes(1,3,0,0,1)$
6404	19_1^-	18.4	$(6,4,0,3)\otimes(1,3,0,0,1)$
		12.0	$(6,4,0,3)\otimes(1,2,0,1,1)$
6712	19_2^-	12.3	$(6,4,2,1)\otimes(1,2,1,0,1)$
		10.3	$(6,4,2,1)\otimes(2,2,0,0,1)$
		10.3	$(6,4,0,3)\otimes(2,2,0,0,1)$
6658	20_1^-	24.1	$(6,4,0,3)\otimes(2,2,0,0,1)$
		12.8	$(6,4,2,1)\otimes(2,2,0,0,1)$

Table III. (*Continued*)

E_{calc} (keV)	J_i^π	Configurations ($\pi \otimes \nu$)	
		%	Leading config.
6780	20_2^-	17.6	$(6,4,0,3)\otimes(0,3,0,1,1)$
		12.5	$(6,4,0,3)\otimes(0,4,0,0,1)$
6795	21_1^-	29.9	$(6,4,0,3)\otimes(1,3,0,0,1)$
		9.1	$(6,4,0,3)\otimes(1,2,0,1,1)$
7278	22_1^-	30.8	$(6,4,0,3)\otimes(1,3,0,0,1)$
		5.7	$(6,4,0,3)\otimes(1,2,0,1,1)$
		5.5	$(4,4,2,3)\otimes(1,3,0,0,1)$
7709	23_1^-	30.2	$(6,4,0,3)\otimes(1,2,0,1,1)$
		16.0	$(6,4,0,3)\otimes(1,3,0,0,1)$
9376	25_1^-	28.2	$(6,4,0,3)\otimes(2,2,0,0,1)$
		18.1	$(6,4,0,3)\otimes(1,2,1,0,1)$

lower-lying negative parity states but involve neutron excitation from the $2d_{5/2}$ orbital to the $1g_{7/2}$ orbital. Except for the 19_2^- state, the 19_1^- to 25_1^- states involve the excitation of two protons from the $2p_{1/2}$ orbital to the $1g_{9/2}$ orbital. The calculated results in the SNE space show that there is no prediction of proton excitation across the shell gap at $Z = 38$.

The overall agreement between the observed states and those predicted by shell model calculations suggests that excitations across the Z=38 subshell gap do not play a significant role up to $I \sim 17\hbar$. However, the higher-spin levels above $I \sim 17\hbar$ are dominated by the excitation of protons over the shell gap at Z=38 into the $1g_{9/2}$ orbital, as shown in Table II. Although the overall agreement between the calculated and measured levels is still far from satisfactory, it is noteworthy that calculations with the GWBXG interaction reproduce the positive parity states well, while those with the SNET interaction match the negative parity states effectively. Our calculations with any single interaction cannot accurately reproduce both positive and negative parity states simultaneously. The observed discrepancies likely arise from outdated interaction models within this mass region, necessitating the recalibration of two-body matrix elements and single-particle energy parameters [25, 41, 45–47]. We believe that the current dataset will assist in developing improved effective interactions tailored for modeling high-spin nuclear states within this regime.

V. CONCLUSIONS

High-spin states of ^{96}Nb were populated via the ^{82}Se(^{18}O,p3n)^{96}Nb reaction at beam energies of 82 and 88 MeV. The previously established level scheme of ^{96}Nb has been significantly expanded with the identification of fourteen new γ rays. Based on the beam-target combinations with the highest neutron-to-proton ratios, most of the γ rays have been assigned spin and parity using ADO and polarization analysis. Shell-model calculations were conducted using two distinct interactions and model spaces to analyze the experimental data for ^{96}Nb. Despite the overall agreement being insufficient, the GWBXG interaction notably aligns with positive-parity states, whereas SNET corresponds better to negative-parity configurations. Current calculations show that no single interaction can precisely reproduce both parity systems simultaneously. The present calculations provide a partial interpretation of the ^{96}Nb spectra. While we cannot definitively assign the observed energy levels, both model spaces indicate that the level sequences primarily reflect single-particle behavior. Valence nucleon excitations outside the ^{88}Sr core dominate the lower and intermediate levels, whereas high-angular-momentum states are driven mainly by proton excitations across the Z=38 subshell. To improve the predictive accuracy of the shell model, it is essential to develop optimized effective interactions for characterizing high-spin nuclear configurations in heavier nuclei.

VI. ACKNOWLEDGMENT

The authors would like to thank the HI-13 tandem accelerator staff for the smooth operation of the machine. We are grateful to Dr. Q. W. Fan for their assistance during target preparation. This work is partially supported by the National Natural Science Foundation of China under Contract No. U2167202, No. U2167201, No. 11975315, and No. U1932209; supported by the Nuclear Technology R&D Program under Grant No. HJSYF2024(01); and supported by the Continuous-Support Basic Scientific Research Project.

[1] X. Z. Cui, L. H. Zhu, X. G. Wu, Z. M. Wang, C. Y. He, Y. Liu, G. S. Li, S. X. Wen, Z. L. Zhang, R. Meng, et al., Phys. Rev. C **72**, 044322 (2005), URL http://link.aps.org/doi/10.1103/PhysRevC.72.044322.

[2] P. W. Luo, X. G. Wu, H. B. Sun, G. S. Li, C. Y. He, Y. Zheng, C. B. Li, S. P. Hu, Y. H. Wu, H. W. Li, et al., Phys. Rev. C **89**, 034318 (2014), URL http://link.aps.org/doi/10.1103/PhysRevC.89.034318.

[3] Y. Zheng, Y. H. Wu, X. G. Wu, C. B. Li, L. H. Zhu, T. X. Li, P. W. Luo, G. S. Li, C. Y. He, H. W. Li, et al., Phys. Rev. C **100**, 014325 (2019), URL https://link.aps.org/doi/10.1103/PhysRevC.100.014325.

[4] Y.-H. Wu, J.-B. Lu, Z. Ren, G.-J. Fu, J. Li, K.-Y. Ma, Y.-J. Ma, X.-G. Wu, Y. Zheng, C.-B. Li, et al., Phys. Rev. C **105**, 034344 (2022), URL https://link.aps.org/doi/10.1103/PhysRevC.105.034344.

[5] Y.-H. Wu, J.-B. Lu, Z. Ren, T.-J. Gao, P.-Y. Yang, Y. Hao, G.-J. Fu, J. Li, K.-Y. Ma, X.-G. Wu, et al., Phys. Rev. C **106**, 054326 (2022), URL https://link.aps.org/doi/10.1103/PhysRevC.106.054326.

[6] Z. Ren, J.-B. Lu, G.-X. Dong, Y. Zheng, Y.-H. Wu, T.-J. Gao, P.-Y. Yang, Y. Hao, K.-Y. Ma, X.-G. Wu, et al., Phys. Rev. C **108**, 044301 (2023), URL http://link.aps.org.https.yzn.proxy.chaoxing.com/doi/10.1103/PhysRevC.108.044301.

[7] Y. Q. Li, C. B. Li, Y. Zheng, T. X. Li, X. G. Wu, R. Hong, S. X. Guan, H. Y. Wu, M. Zheng, Z. H. Zhao, et al., Phys. Rev. C **110**, 054309 (2024), URL

https://link_aps_org.ciae.vpn358.com/doi/10.1103/PhysRevC.110.054309.

[8] Y.-H. Wu, J.-B. Lu, Z. Ren, G.-J. Fu, C.-Q. Li, P.-Y. Yang, Y. Hao, T.-J. Gao, L.-H. Zhu, X.-Z. Cui, et al., Phys. Rev. C **109**, 024326 (2024), URL https://link.aps.org/doi/10.1103/PhysRevC.109.024326.

[9] B. Kern, T. Fényes, A. Krasznahorkay, Z. Dombrádi, S. Brant, and V. Paar, Nuclear Physics A **430**, 301 (1984), ISSN 0375-9474, URL https://www.sciencedirect.com/science/article/pii/0375947484900423.

[10] S. Cochavi and D. B. Fossan, Phys. Rev. C **5**, 164 (1972), URL https://link.aps.org/doi/10.1103/PhysRevC.5.164.

[11] P. F. Cloessner, W. Stöffl, R. K. Sheline, and R. G. Lanier, Phys. Rev. C **29**, 657 (1984), URL https://link.aps.org/doi/10.1103/PhysRevC.29.657.

[12] J. H. Thies, P. Puppe, T. Adachi, M. Dozono, H. Ejiri, D. Frekers, H. Fujita, Y. Fujita, M. Fujiwara, E.-W. Grewe, et al., Phys. Rev. C **86**, 054323 (2012), URL https://link.aps.org/doi/10.1103/PhysRevC.86.054323.

[13] J. R. Comfort, J. V. Maher, G. C. Morrison, and J. P. Schiffer, Phys. Rev. Lett. **25**, 383 (1970), URL https://link.aps.org/doi/10.1103/PhysRevLett.25.383.

[14] M. S. Zusman and B. G. Harvey, Phys. Rev. C **5**, 1031 (1972), URL http://link.aps.org/doi/10.1103/PhysRevC.5.1031.

[15] N. Fotiades, J. A. Cizewski, R. Krücken, R. M. Clark, P. Fallon, I. Y. Lee, A. O. Macchiavelli, J. A. Becker, and W. Younes, Phys. Rev. C **82**, 044306 (2010), URL https://link.aps.org/doi/10.1103/PhysRevC.82.044306.

[16] V. Kumar, R. Chapman, D. O'Donnell, J. Ollier, R. Orlandi, J. F. Smith, K.-M. Spohr, D. A. Torres, P. Wady, S. K. Tandel, et al., Phys. Rev. C **108**, 044313 (2023), URL http://link.aps.org.https.yzn.proxy.chaoxing.com/doi/10.1103/PhysRevC.108.044313.

[17] H. Wu, Z. Li, H. Tan, H. Hua, J. Li, W. Hennig, W. Warburton, D. Luo, X. Wang, X. Li, et al., Nuclear Instruments and Methods in Physics Research Section A: Accelerators, Spectrometers, Detectors and Associated Equipment **975**, 164200 (2020), ISSN 0168-9002, URL https://www.sciencedirect.com/science/article/pii/S0168900220305969.

[18] D.-W. Luo, H.-Y. Wu, Z.-H. Li, C. Xu, H. Hua, X.-Q. Li, X. Wang, S.-Q. Zhang, Z.-Q. Chen, C.-G. Wu, et al., Nuclear Science and Techniques **32**, 79 (2021), URL https://link.springer.com/article/10.1007/s41365-021-00917-8.

[19] D. Radford, Nuclear Instruments and Methods in Physics Research Section A: Accelerators, Spectrometers, Detectors and Associated Equipment **361**, 297 (1995), ISSN 0168-9002, URL http://www.sciencedirect.com/science/article/pii/0168900295001832.

[20] C. Droste, S. Rohoziński, K. Starosta, T. Morek, J. Srebrny, and P. Magierski, Nuclear Instruments and Methods in Physics Research Section A: Accelerators, Spectrometers, Detectors and Associated Equipment **378**, 518 (1996), ISSN 0168-9002, URL https://www.sciencedirect.com/science/article/pii/0168900296004263.

[21] G. Duchêne, F. Beck, P. Twin, G. de France, D. Curien, L. Han, C. Beausang, M. Bentley, P. Nolan, and J. Simpson, Nuclear Instruments and Methods in Physics Research Section A: Accelerators, Spectrometers, Detectors and Associated Equipment **432**, 90 (1999), ISSN 0168-9002, URL https://www.sciencedirect.com/science/article/pii/S0168900299002776.

[22] K. Starosta, T. Morek, C. Droste, S. Rohoziński, J. Srebrny, A. Wierzchucka, M. Bergström, B. Herskind, E. Melby, T. Czosnyka, et al., Nuclear Instruments and Methods in Physics Research Section A: Accelerators, Spectrometers, Detectors and Associated Equipment **423**, 16 (1999), ISSN 0168-9002, URL https://www.sciencedirect.com/science/article/pii/S0168900298012200.

[23] N. Mărginean, D. Bucurescu, G. C ăta Danil, I. C ăta Danil, M. Ivaşcu, and C. A. Ur, Phys. Rev. C **62**, 034309 (2000), URL https://link.aps.org/doi/10.1103/PhysRevC.62.034309.

[24] J. K. Hwang, A. V. Ramayya, J. H. Hamilton, Y. X. Luo, J. O. Rasmussen, C. J. Beyer, P. M. Gore, S. C. Wu, I. Y. Lee, C. M. Folden, et al., Phys. Rev. C **67**, 014317 (2003), URL https://link.aps.org/doi/10.1103/PhysRevC.67.014317.

[25] J. M. Chatterjee, M. Saha-Sarkar, S. Bhattacharya, S. Sarkar, R. P. Singh, S. Murulithar, and R. K. Bhowmik, Phys. Rev. C **69**, 044303 (2004), URL https://link.aps.org/doi/10.1103/PhysRevC.69.044303.

[26] P. Dey, R. Palit, P. C. Srivastava, B. Das, A. Kundu, M. S. R. Laskar, V. Malik, D. Negi, and S. Sharma, Phys. Rev. C **109**, 034313 (2024), URL https://link.aps.org/doi/10.1103/PhysRevC.109.034313.

[27] B. Brown and W. Rae, Nuclear Data Sheets **120**, 115 (2014), ISSN 0090-3752, URL http://www.sciencedirect.com/science/article/pii/S0090375214004748.

[28] R. Gross and A. Frenkel, Nuclear Physics A **267**, 85 (1976), ISSN 0375-9474, URL http://www.sciencedirect.com/science/article/pii/037594747690645X.

[29] J. Blomqvist and L. Rydström, Physica Scripta **31**, 31 (1985), URL http://stacks.iop.org/1402-4896/31/i=1/a=006.

[30] P. Li, W. Daehnick, S. K. Saha, J. Brown, and R. Kouzes, Nuclear Physics A **469**, 393 (1987), ISSN 0375-9474, URL http://www.sciencedirect.com/science/article/pii/0375947487900285.

[31] E. A. Stefanova, R. Schwengner, J. Reif, H. Schnare, F. Dönau, M. Wilhelm, A. Fitzler, S. Kasemann, P. von Brentano, and W. Andrejtscheff, Phys. Rev. C **62**, 054314 (2000), URL http://link.aps.org/doi/10.1103/PhysRevC.62.054314.

[32] E. A. Stefanova, M. Danchev, R. Schwengner, D. L. Balabanski, M. P. Carpenter, M. Djongolov, S. M. Fischer, D. J. Hartley, R. V. F. Janssens, W. F. Mueller, et al., Phys. Rev. C **65**, 034323 (2002), URL https://link.aps.org/doi/10.1103/PhysRevC.65.034323.

[33] S. S. Ghugre and S. K. Datta, Phys. Rev. C **52**, 1881 (1995), URL http://link.aps.org/doi/10.1103/PhysRevC.52.1881.

[34] G. S. Simpson, W. Urban, K. Sieja, J. A. Dare, J. Jolie, A. Linneman, R. Orlandi, A. Scherillo, A. G. Smith, T. Soldner, et al., Phys. Rev. C **82**, 024302 (2010), URL https://link.aps.org/doi/10.1103/PhysRevC.82.024302.

[35] H. Blok, W. Zimmerman, J. Kraushaar, and P. Batay-Csorba, Nuclear Physics A **287**, 156 (1977), ISSN 0375-9474, URL https://www.sciencedirect.com/science/article/pii/0375947477905693.

[36] E. A. Stefanova, M. Danchev, R. Schwengner, D. L. Balabanski, M. P. Carpenter, M. Djongolov, S. M. Fischer, D. J. Hartley, R. V. F. Janssens, W. F. Mueller, et al., Phys. Rev. C **65**, 034323 (2002), URL https://link.aps.org/doi/10.1103/PhysRevC.65.034323.

[37] T. Rząca-Urban, K. Sieja, W. Urban, F. Nowacki, J. L.

Durell, A. G. Smith, and I. Ahmad, Phys. Rev. C **79**, 024319 (2009), URL https://link.aps.org/doi/10.1103/PhysRevC.79.024319.

[38] W. Urban, K. Sieja, T. Rząca-Urban, J. Wiśniewski, A. Blanc, M. Jentschel, P. Mutti, U. Köster, T. Soldner, G. de France, et al., Phys. Rev. C **104**, 064309 (2021), URL https://link.aps.org/doi/10.1103/PhysRevC.104.064309.

[39] K. Sieja, Universe **8** (2022), ISSN 2218-1997, URL https://www_mdpi_com.ciae.vpn358.com/2218-1997/8/1/23.

[40] W. Urban, K. Sieja, G. S. Simpson, H. Faust, T. Rząca-Urban, A. Złomaniec, M. Łukasiewicz, A. G. Smith, J. L. Durell, J. F. Smith, et al., Phys. Rev. C **79**, 044304 (2009), URL https://link.aps.org/doi/10.1103/PhysRevC.79.044304.

[41] K. Sieja, F. Nowacki, K. Langanke, and G. Martínez-Pinedo, Phys. Rev. C **79**, 064310 (2009), URL https://link_aps_org.ciae.vpn358.com/doi/10.1103/PhysRevC.79.064310.

[42] E. Gregor, M. Scheck, R. Chapman, L. Gaffney, J. Keatings, K. Mashtakov, D. O'Donnell, J. Smith, P. Spagnoletti, M. Thürauf, et al., The European Physical Journal A **53**, 1 (2017), URL https://link.springer.com/article/10.1140/epja/i2017-12224-7.

[43] T. Rząca-Urban, W. Urban, A. Blanc, M. Jentschel, P. Mutti, U. Köster, G. de France, G. S. Simpson, and C. A. Ur, Phys. Rev. C **108**, 014324 (2023), URL https://link_aps_org.ciae.vpn358.com/doi/10.1103/PhysRevC.108.014324.

[44] B. Brown and W. Rae, Nuclear Data Sheets **120**, 115 (2014), ISSN 0090-3752, URL https://www.sciencedirect.com/science/article/pii/S0090375214004748.

[45] A. Holt, T. Engeland, M. Hjorth-Jensen, and E. Osnes, Phys. Rev. C **61**, 064318 (2000), URL https://link.aps.org/doi/10.1103/PhysRevC.61.064318.

[46] M. Honma, T. Otsuka, T. Mizusaki, and M. Hjorth-Jensen, Phys. Rev. C **80**, 064323 (2009), URL https://link.aps.org/doi/10.1103/PhysRevC.80.064323.

[47] D. K. Sharp, B. P. Kay, J. S. Thomas, S. J. Freeman, J. P. Schiffer, B. B. Back, S. Bedoor, T. Bloxham, J. A. Clark, C. M. Deibel, et al., Phys. Rev. C **87**, 014312 (2013), URL https://link.aps.org/doi/10.1103/PhysRevC.87.014312.